

Engineering heat transport across epitaxial lattice-mismatched van der Waals heterointerfaces

Emigdio Chavez-Angel,¹ Polychronis Tsipas,² Peng Xiao,¹ Mohammad Taghi Ahmadi,³ Abdalghani Daaoub,³ Hatef Sadeghi,³ Clivia M. Sotomayor Torres,^{1,4} Athanasios Dimoulas² and Alexandros El Sachat^{1,2}*

¹ Catalan Institute of Nanoscience and Nanotechnology (ICN2), CSIC and BIST, Campus UAB, Bellaterra, 08193 Barcelona, Spain

² Institute of Nanoscience and Nanotechnology, National Center for Scientific Research “Demokritos,” 15341 Agia Paraskevi, Athens, Greece

³ School of Engineering, University of Warwick, Coventry CV4 7AL, United Kingdom

⁴ ICREA, Passeig Lluís Companys 23, 08010 Barcelona, Spain

*Corresponding author: a.elsachat@inn.demokritos.gr

Abstract. Artificially engineered 2D materials offer unique physical properties for thermal management, surpassing naturally occurring materials. Here, using van der Waals epitaxy, we demonstrate the ability to engineer extremely insulating ultra-thin thermal metamaterials based on crystalline lattice-mismatched Bi₂Se₃/MoSe₂ superlattices and graphene/PdSe₂ heterostructures with exceptional thermal resistances (70–202 m²K/GW) and ultralow cross-plane thermal conductivities (0.01–0.07 W/mK) at room temperature, comparable to those of amorphous

materials. Experimental data obtained using frequency-domain thermoreflectance and low-frequency Raman spectroscopy, supported by tight-binding phonon calculations, reveal the impact of lattice mismatch, phonon-interface scattering, size effects, temperature and interface thermal resistance on cross-plane heat dissipation, uncovering different thermal transport regimes and the dominant role of long-wavelength phonons. Our findings provide essential insights into emerging synthesis and thermal characterization methods and valuable guidance for the development of large-area heteroepitaxial van der Waals films of dissimilar materials with tailored thermal transport characteristics.

The recent advent of van der Waals (vdW) heterostructures and superlattices (SLs) has opened new perspectives in nanoelectronics with ultra-high mobility and topological properties, in optics with high absorption and sensitivity, as well as in the field of heat transport engineering, with low scattering rates and highly anisotropic properties.¹⁻⁴ Specifically, thermodynamically stable misfit layer compounds, vdW heterostructures and SLs with tailored thermal transport and thermoelectric conversion properties have been recently proposed for thermal management applications.⁴⁻⁸ Due to the periodic nature of SLs, new phonon modes and bandgaps can be formed due to the folding effect, which results in strong modifications of the phonon group velocity and thermal conductivity depending on the period thickness.⁹ More interestingly, vdW SLs assembled from layers with structural lattice mismatch and weak vdW interactions could enable strong reduction of phonon transport along the *c*-axis while retaining their in-plane crystallinity.

Despite significant efforts toward this direction, many experimental studies have reported vdW stacks using top-down fabrication methods, such as exfoliation, which can only prepare small flakes on a micrometer scale.^{8,10-12} Additionally, such flakes is most likely to have defects or

contamination. Nevertheless, Vaziri et al.¹² and Sood et al.⁸ have demonstrated high thermal isolation across a few micrometer size exfoliated Gr/MoSe₂/MoS₂/WSe₂ heterostructures and graphene/MoS₂ SLs, respectively. In addition, Kim et al. have achieved ultra-low cross-plane thermal conductivity at room temperature (~ 0.041 W/mK) using van der Waals films with random interlayer rotations, but exclusively in polycrystalline WS₂ films.¹³ In contrast, bottom-up epitaxial techniques, such as molecular beam epitaxy (MBE), enable the fabrication of high-order vdW SLs at wafer scale with atomically smooth and abrupt periodic interfaces.^{1,14-16} The ability to control atomic layer thickness and chemical composition also allows the precise designing of the transport properties of the SLs. Moreover, due to the weak vdW interactions between layers, vdW epitaxy offers great flexibility for integrating atomic layers of distinct materials such as metals, semiconductors, superconductors, or insulators, without considering lattice-matching requirements.^{1,17}

Here, using wafer-scale heteroepitaxial growth we demonstrate superior cross-plane thermal insulation based on atomically-thin crystalline vdW layered materials. Specifically, we directly grow on different substrates high quality lattice-mismatched Bi₂Se₃/MoSe₂ SLs and graphene/PdSe₂ heterostructures of varying thickness that exhibit tailored thermal transport properties at the atomic-scale. Combining contactless characterization techniques, e.g., frequency-domain thermoreflectance (FDTR) and low-frequency Raman spectroscopy, we study the acoustic and thermal properties of these epitaxial films. We focus on unraveling the impact of vibrational mismatch, phonon-interface scattering, temperature and film thickness on cross-plane thermal transport and we estimate the effective cross-plane thermal conductivity and total thermal resistance of the films taking into account all the interfacial contributions in our multilayer structures. Phonon transport calculations support our experimental data and further reveal the

impact of the thermal contact resistance on thermal conduction of ultra-thin layered materials and the presence of different thermal transport regimes in such atomically thin 2D films. Until today, only the in-plane thermal transport properties of Bi_2Se_3 , MoSe_2 and PdSe_2 films have been investigated,¹⁸⁻²² while such high cross-plane thermal insulating properties have been achieved only using either polycrystalline films consisting of a single material or exfoliated vdW stacks.

Results

We grew the epitaxial Bi_2Se_3 films, $\text{Bi}_2\text{Se}_3/\text{MoSe}_2$ SLs and graphene/ PdSe_2 heterostructures on various single-crystal substrates such as strontium titanate (STO), sapphire and silicon carbide (SiC) by MBE, yielding 2D thin films with minimal disorder. A schematic representation of each vdW material is shown in Fig. 1a-c. The structural and chemical characterization of the samples were studied by X-ray Photoelectron Spectroscopy (XPS), low-frequency Raman spectroscopy, scanning tunnelling microscopy (STM) and high resolution scanning transmission electron microscopy (HR-STEM) measurements. Figure 1d displays HR-STEM images of different thickness $\text{Bi}_2\text{Se}_3/\text{MoSe}_2$ SLs that confirm the expected layering structures, which consist of vertically stacked Bi_2Se_3 and MoSe_2 sublayers with atomically sharp and contamination-free interfaces. Reflection high-energy electron diffraction (RHEED) patterns show that MoSe_2 and Bi_2Se_3 layers are repeatedly grown highly oriented on top of each other despite their large lattice mismatch ($\sim 20\%$) (see also Fig. S1 in Supporting Information (SI)). The RHEED patterns of one quintuple layer (QL) Bi_2Se_3 and $\text{Bi}_2\text{Se}_3/\text{MoSe}_2$ heterostructure (Fig. 1e-h) show the difference in the relative positions of the streaks, which reflects the large lattice mismatch between Bi_2Se_3 and MoSe_2 at room temperature.

In situ XPS data for the Bi_2Se_3 thin films and $\text{Bi}_2\text{Se}_3/\text{MoSe}_2$ heterostructures are presented in Fig. 1k-n. The binding energies of the Bi $4f_{7/2}$ and Se $3d_{5/2}$ core levels for 1 QL Bi_2Se_3 grown

directly on STO were 158.00 eV and 53.71 eV, respectively, in good agreement with previous reported²³ on thin-film single crystal Bi₂Se₃. After 2 ML MoSe₂ growth, the Mo 3d_{5/2} and Se 3d_{5/2} peak positions at 228.54 eV and 54.25 eV, respectively, indicate Mo-Se bonds and agreed well with the MoSe₂ formation.²⁴ The Se 3d peak in Fig. 1n is deconvoluted in four peaks to consider two types of bonds, namely, Bi-Se and Mo-Se bonds, keeping the Se 3d_{5/2}-3d_{3/2} spin-orbit splitting fixed at 0.86 eV. The two distinct Se environments suggest Bi₂Se₃ and MoSe₂ formation rather than the formation of a mixed Bi-Mo-Se compound. The latter is reinforced by the fact that the Bi 4f_{7/2} peak position remains the same after MoSe₂ film growth (see Fig. S2 in SI). The XPS spectra from the graphene/PdSe₂ heterostructures are shown in the SI (Fig. S3).

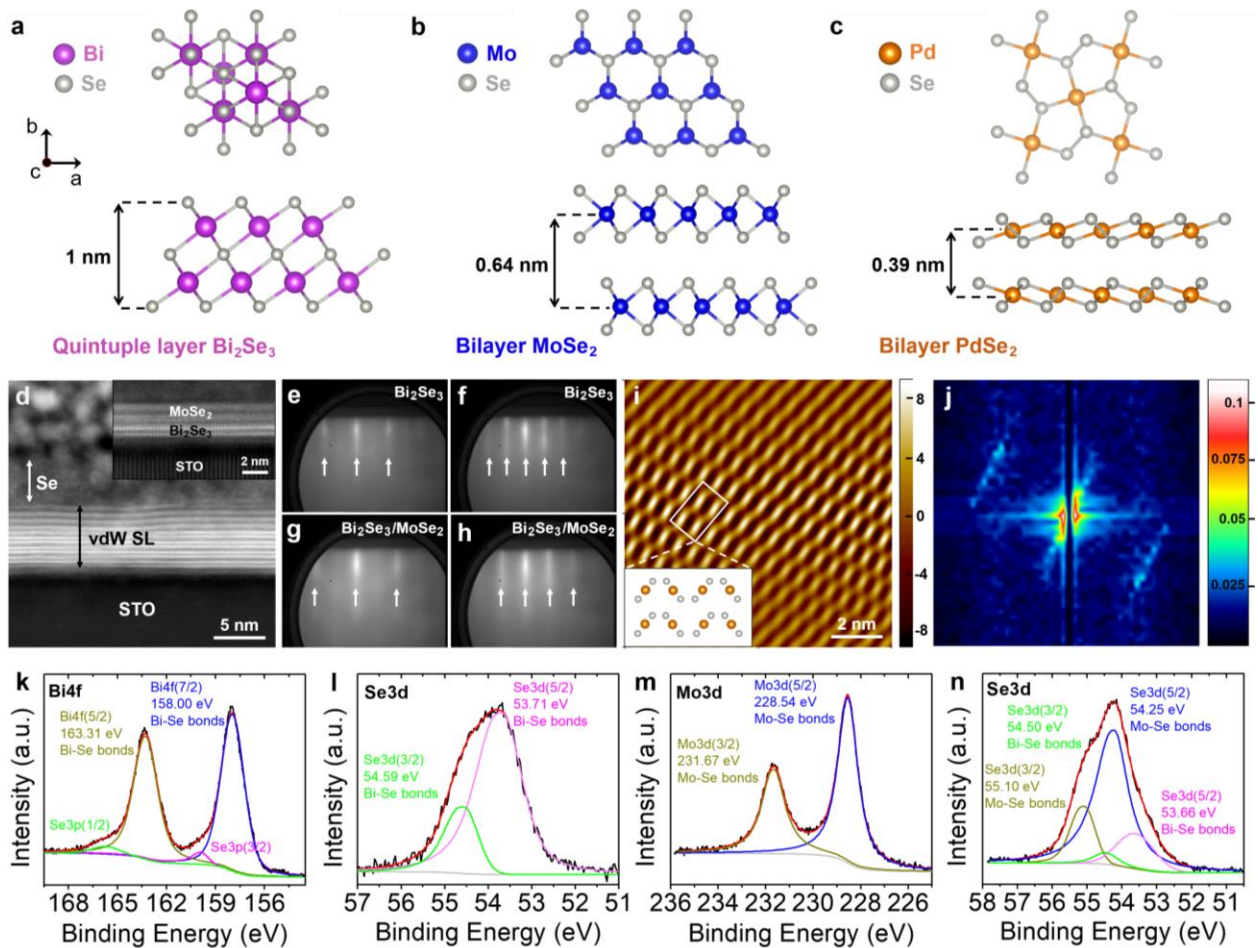


Fig. 1. Structural and chemical characterization of epitaxial vdW films. Top and side views of (a) Bi₂Se₃, (b) MoSe₂ and (c) PdSe₂ crystal structures. The purple, blue and orange spheres represent Bi, Mo and Pd atoms, respectively, while Se atoms are shown with grey spheres. 1 QL Bi₂Se₃ consists of five atoms per unit cell, such as Se-Bi-Se-Bi-Se, while each monolayer MoSe₂ consists of three atomic sublayers, in which Mo atoms are sandwiched between Se atoms. In PdSe₂, each Pd atom is connected with four Se atoms, and each Se atom is bonded with two Pd atoms and another Se atom. (d) Cross-sectional STEM images of the as-synthesized vdW Bi₂Se₃/MoSe₂ SLs with periods $n = 3$ and $n = 1$ (inset figure) on STO substrates. After the growth, a 4 nm thick Se capping layer was deposited in situ to protect the SL from oxidation. RHEED patterns of 1 QL Bi₂Se₃ and Bi₂Se₃/MoSe₂ SL with period $n=1$ along the (e), (g) [11–20] and (f), (h) [11–10] azimuths. (i) STM image of the as grown monolayer PdSe₂ on graphene and (j) the corresponding fast Fourier transform (FFT) image of the whole region. (k-n). XPS data of Bi₂Se₃/MoSe₂ SL grown on STO substrates.

Next, we systematically study the phonon properties of Bi₂Se₃ films, Bi₂Se₃/MoSe₂ SLs and graphene/PdSe₂ heterostructures using low-frequency Raman spectroscopy. Figure 2a shows the Raman spectra of Bi₂Se₃ films of varying thickness (from 1 to 20 QL), where all the out and in-plane Raman active optical modes are observed ($2E_g$ and $2A_{1g}$). Specifically, the E_{1g}^1 , E_g^2 , A_{1g}^1 and A_{1g}^2 modes are detected at ~ 37 cm⁻¹, ~ 132 cm⁻¹, ~ 71 cm⁻¹ and ~ 173 cm⁻¹, respectively, in agreement with previous studies.^{25,26} Both out-of-plane modes (A_{1g}^1 , A_{1g}^2) show a pronounced red shift (about 2.7 cm⁻¹) as the thickness decreases; while the in-plane modes (E_{1g}^1 , E_g^2) are red-shifted with decreasing thickness of about 1.7 and 3.5 cm⁻¹, respectively (see also Fig. S11a). We note that the A_{1g}^1 is more sensitive with thickness because it reflects the out-of-plane vibrations of the Se and Bi atoms.²⁶ We also observe a broadening of the E_g^2 mode as the film thickness decreases

(see Fig. 2a), in agreement with previous reports,²⁶ suggesting that the layer-to-layer stacking strongly affects the interlayer bonding. In SLs (see Fig. 2b) except of the Raman modes that correspond to Bi₂Se₃, we detect the A_{1g} mode in the spectral range of 240.1–241.1 cm⁻¹, which confirms the existence of MoSe₂ layers.^{27,28} In Figure 2c we also plot the ratios of the Raman intensities for the out-of-plane (I_{A_{1g}¹}/I_{A_{1g}²}) and in-phase shear modes (I_{E_g¹}/I_{E_g²}) of the adjacent layers versus thickness for the case of Bi₂Se₃ films and Bi₂Se₃/MoSe₂ SLs for direct comparison. We find that for the case of Bi₂Se₃ films, both I_{A_{1g}¹}/I_{A_{1g}²} and I_{E_g¹}/I_{E_g²} ratios decrease with decreasing thickness of less than 3 nm, in agreement with a previous study.²⁶ In the SLs, the values of the ratios I_{A_{1g}¹}/I_{A_{1g}²} and I_{E_g¹}/I_{E_g²} are similar to those calculated in Bi₂Se₃ films and remain almost constant with decreasing period.

In graphene/PdSe₂ heterostructures, we detected 6 main peaks in the high-frequency region (>130 cm⁻¹) that belong to A_g¹, B_{1g}¹, A_g², B_{1g}², A_g³ and B_{1g}³ phonon modes of PdSe₂ (Fig. 2d). These modes can be attributed to the intralayer vibrations of PdSe₂. The Raman peak positions of all phonon modes showed a red shift with increasing the number of layers, in agreement with previous CVD grown PdSe₂ films.^{29,30} Interestingly, the intralayer vibration at 149.1 cm⁻¹, originating from the intralayer Se–Se bonds, exhibits sufficiently strong Raman intensity in 3, 5, and 7L PdSe₂, indicating its strong coupling to the electronic states.²⁹ Furthermore, we observe Raman-inactive modes in the frequency region between 50–130 cm⁻¹, which are activated due to the breakdown of translation symmetry in few layers, as has been recently shown.^{30,31} The phonon modes detected in the frequency region between 100 to 300 cm⁻¹ are also consistent with a recent study where graphene/PdSe₂ heterostructures have been formed by exfoliation.³² Finally, the two Raman peaks, SiC₁ and SiC₂ with 196.6 cm⁻¹ and 204.3 cm⁻¹, respectively, originated from the undoped SiC

substrate.³³ We note that the mode A_g^2 is not well visible because it partially overlaps with the SiC₂ mode.

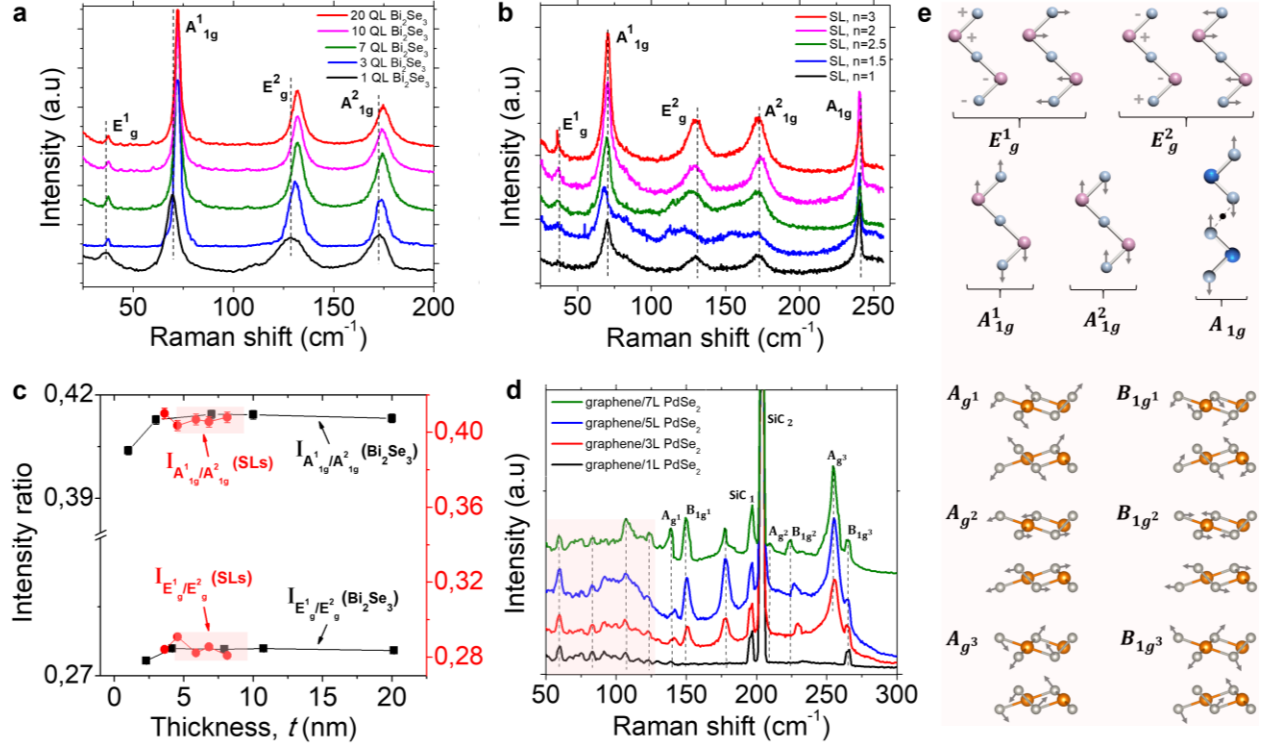


Fig. 2. Low-frequency Raman spectroscopy in epitaxial vdW films. Raman scattering spectra in (a) Bi₂Se₃ films of different thickness and (b) Bi₂Se₃/MoSe₂ SLs. (c) Ratios of the Raman intensities for the out-of-plane ($I_{A_{1g}^1}/I_{A_{1g}^2}$) and in-phase shear modes ($I_{E_g^1}/I_{E_g^2}$) versus film thickness for the case of Bi₂Se₃ films (black squares) and Bi₂Se₃/MoSe₂ SLs (red circles). (d) Low-frequency Raman scattering spectra in graphene/PdSe₂ heterostructures of different thicknesses. The red-shaded area shows the frequency region where the Raman-inactive modes are detected. (e) Atomic displacements (grey arrows) of all the Raman modes detected in Bi₂Se₃ films, Bi₂Se₃/MoSe₂ SLs and graphene/PdSe₂ heterostructures. The purple, blue and orange spheres represent Bi, Mo and Pd atoms, respectively, while Se atoms are shown with grey spheres.

The thermal measurements were performed using our custom-built frequency-domain thermoreflectance (FDTR) setup, which essentially combines simultaneous measurements of cross-plane thermal conductivity (k_z) and interface thermal conductance.^{34,35} For the case of SLs, our multilayer structures consist of Au/SLs/substrate stacks (see Fig. 3a). For each SL, we obtained FDTR measurements and extracted the effective k_z and the interface thermal resistances between Au (transducer)/SL (R_1) and SL/substrate (R_2) following a multilayer three-dimensional heat diffusion model.³⁶ The required material properties for this model are the thickness (t), the volumetric heat capacity (C), R_1 , R_2 and k_z . The thermal conductivity and volumetric heat capacity of Au as well as the volumetric specific heat of Bi_2Se_3 and MoSe_2 were taken from the literature.^{37,38} Therefore, the unknown parameters are the k_z , R_1 and R_2 . To estimate these three parameters, first we quantified the sensitivity of the recorded phase signal to different parameters according to our multilayer geometry (see Fig. S4 in SI), following a similar methodology as reported elsewhere.³⁴⁻³⁶

Typical examples of the recorded phase signal and the corresponding best model fits in bilayer MoSe_2 and $\text{Bi}_2\text{Se}_3/\text{MoSe}_2$ SLs with periods 2, 2.5 and 3 are shown in Fig. 3b. To extract the k_z of each SL from a single measurement, we followed the same approach that used in previous works,^{34-36,39} and supported by our sensitivity analysis. First, we extract k_z by fitting the experimental data in a low frequency range (20 kHz to 1 MHz), where the phase signal sensitivity to R_1 , R_2 , and C of the films is negligible. Then, we fix k_z and fit the high frequency range (1–45 MHz) to estimate R_1 and R_2 . The same procedure was followed to extract k_z , R_1 and R_2 for all the epitaxial films. The sensitivity analysis and FDTR data for the case of graphene/ PdSe_2 are shown in Fig. S5 and Fig. S6, respectively. In Figure S9, we also show all the interface thermal resistance values,

$R_{\text{int}} = R_1 + R_2$, where $R_1 = 1/G_1$ and $R_2 = 1/G_2$ extracted by the FDTR experiments and compare them with previous reports.

In SLs, we observe that k_z slightly increases with increasing thickness with values between 0.059–0.07 W/mK (see Fig. 3c). However, in graphene/PdSe₂ heterostructures, we found a strong thickness-dependent k_z . Specifically, the k_z increased by a factor of six with increasing the thickness of the top PdSe₂ layers from one to seven layers. To confirm the robustness of our approach to measuring the intrinsic k_z of ultra-thin films, we performed FDTR measurements in Bi₂Se₃ films of different thicknesses in both STO and sapphire substrates. We found that in both substrates the k_z of the Bi₂Se₃ films increases by a factor of five with increasing thickness from 1 to 20 QL. The excellent agreement in k_z values is shown in Figure 3c.

The origin of the weak thickness dependence of the k_z in SLs can be understood considering both interface-phonon scattering and size effects. By increasing the film thickness, thus the period of the SLs, thermal phonons (especially short-wavelength) are scattered by multiple Bi₂Se₃-MoSe₂ interfaces, thus reducing their contribution to cross-plane thermal transport. In contrast, the increase in the volume fraction of the constituents of the SLs with increasing thickness allows more long-wavelength phonons to propagate and contribute to k_z until they are scattered at the sample boundaries. These opposite effects resulted in the suppressed thickness-dependent k_z trend presented in Fig. 3c. Therefore, despite the influence of interface phonon scattering on k_z , the apparent increase of k_z with increasing thickness in SLs indicates that in this thickness range finite size effects are still dominant. This is in agreement with previous studies that showed that the transmission of phonons across short-period AlN/GaN⁴⁰ and SiGe^{41,42} SLs strongly depends on the phonon wavelength, suggesting that long-wavelength phonons are the dominant carriers of heat.

Molecular dynamics simulations have also shown that the k_z of SLs with lattice-mismatched interfaces increases monotonically with period length.⁴³

However, the absence or limited interfaces in pure Bi_2Se_3 and graphene/ PdSe_2 allow the majority of the thermally excited phonons to contribute to cross-plane thermal transport, i.e., k_z is limited mainly by finite size effects. This is reflected in the different rates of increase of k_z observed in Fig. 3c. In particular, for the same thickness range, in $\text{Bi}_2\text{Se}_3/\text{MoSe}_2$ SLs, we found only a 28% of increase in k_z with increasing thickness while in Bi_2Se_3 and graphene/ PdSe_2 films of about 42% and 68%, respectively. We note that to study coherent and incoherent effects in SLs, the volume fraction of the constituents and total thickness of the films should remain constant while the thickness of each layer in a period must be adjusted to vary the interface density.¹⁶ Therefore, in our SLs, the apparent linear scale of k_z vs period is not sufficient to conclude if phonons travel coherently across the film thickness. For instance, previous calculations showed that despite the linear k_z increase with thickness, lattice mismatch destroys the Bragg reflection conditions and phonons are diffusely scattered at interfaces, thus losing their coherency.⁴³

To quantify the impact of cross-plane ballistic phonon transport on the total thermal resistance in our epitaxial films, we estimate the total thermal resistance per unit area, R_{tot} , which can be written as the sum of the combined interface thermal resistance, $R_{\text{int}} = R_1 + R_2$, and volumetric cross-plane thermal resistance, $R_{\text{film}} = t/k_z$.^{34,44} From these calculations, we found that in the SLs R_{tot} is linearly proportional to the total thickness (or number of periods, n), such that $R_{\text{tot}, n=3} > R_{\text{tot}, n=2,5} > R_{\text{tot}, n=2} > R_{\text{tot}, n=1,5} > R_{\text{tot}, n=1}$ (Fig. 3d). Furthermore, we observe that R_{int} increases with increasing the period of the SLs (Fig. S9), in agreement with previous thermal resistance measurements in short-period SLs.^{8,40} We note that the large lattice-mismatch between Bi_2Se_3 and MoSe_2 (~20%) most likely enhances the phonon interface scattering and further contributes to the

increased values of R_{tot} . This is in agreement with previous studies that showed that lattice-mismatched interfaces exhibit reduced interface thermal conductance and phonon transmission due to the increased lattice disorder.^{45,46}

However, in graphene/PdSe₂ heterostructures R_{tot} remains constant with increasing the thickness of PdSe₂ from 1 to 7 layers. In fact, the different slopes in Fig. 3d suggest different thermal transport regimes. The similar values of R_{tot} in graphene/PdSe₂ indicate strong ballistic thermal transport, as it is expected in a thin film with no internal scattering.⁴⁷ Similarly, cross-plane ballistic thermal transport has been found in graphene,⁴⁸ MoS₂⁴⁴ and PtSe₂³⁴ thin films. However, the increased values of the R_{tot} with increasing thickness observed in SLs indicate additional phonon scattering (quasi-ballistic regime). We attribute this result to the scattering of high-frequency phonons at multiple Bi₂Se₃/MoSe₂ interfaces, which largely disrupt phonon ballistic transport. Therefore, interface roughness and lattice mismatch are effective in destroying the coherence of high-frequency phonons.

In Fig. 3d we show all our calculated R_{tot} values and compare them with previous R_{tot} measurements on different 2D materials and SLs, where similar interfacial contributions from bottom (2D material/substrate) and top (metal/2D material) interfaces were considered.^{8,48} In Fig. S12 in SI, we also plot the volumetric cross-plane thermal resistance, R_{film} , as a function of thickness t , which further supports the previous discussion. Specifically, we observe that the R_{film} is increasing by more than a factor of two as the thickness increases from 1.4 to 7.2 nm, which further suggests quasi-ballistic phonon transport and phonon diffusive scattering at interfaces. Notably, in ultra-thin graphene/PdSe₂ stacks, R_{film} saturates at a finite value of about 54 m²K/GW, .i.e., ballistic thermal transport. Similarly, Sood et al. using density functional theory (DFT) calculations, have estimated a constant cross-plane ballistic thermal resistance of ~10 m²K/GW in

MoSe₂ films in the limit of 2–3 monolayers.⁴⁴ The significant contributions of both R_{film} and R_{int} components to the R_{tot} in all the epitaxial films suggest that interfacial effects do not entirely govern cross-plane thermal transport.

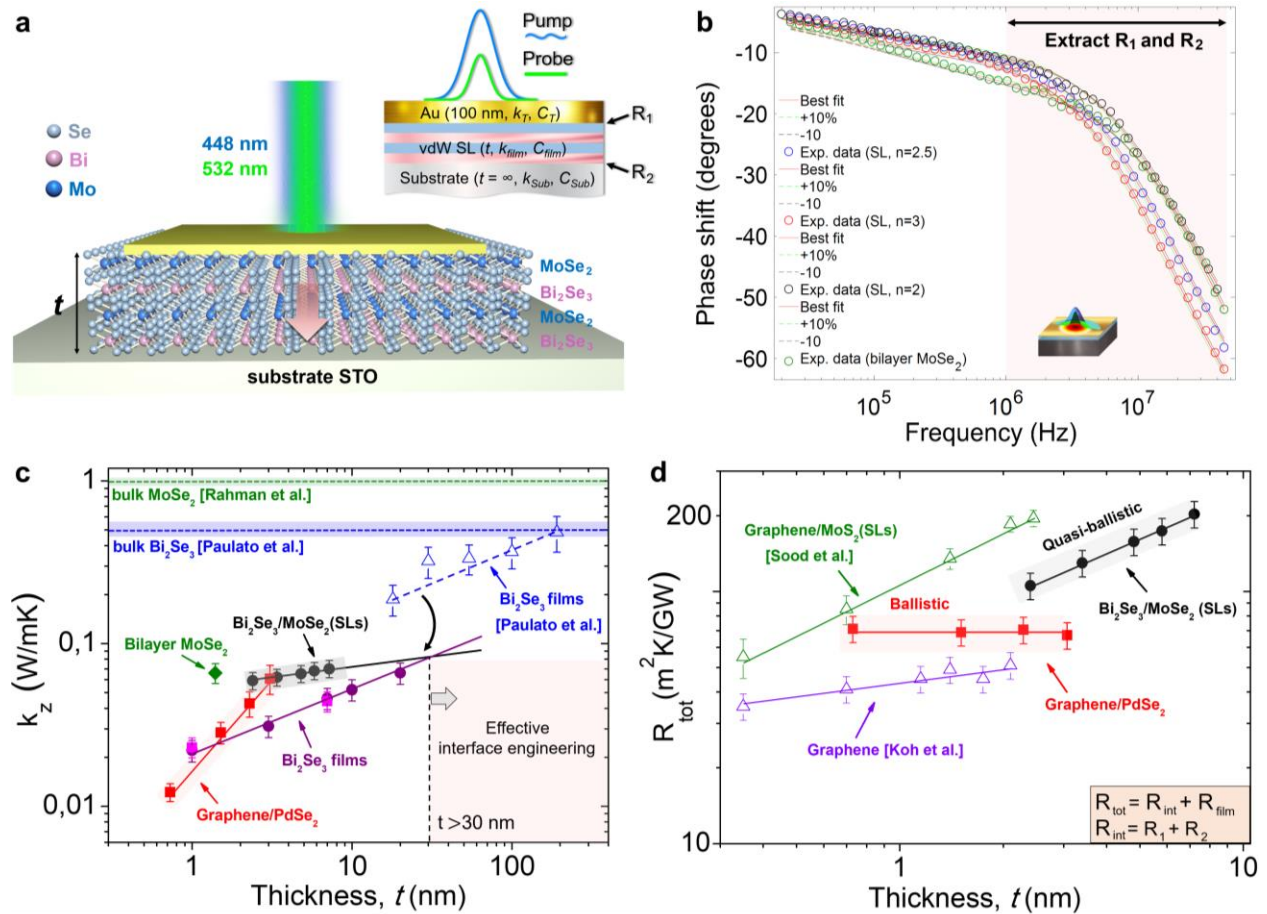


Fig. 3. Thermal conductivity and interfacial heat transport measurements. (a) Schematic illustrations of the FDTR technique and the multilayer system of the SLs. (b) Typical FDTR data measured in bilayer MoSe₂ and Bi₂Se₃/MoSe₂ SLs with periods $n = 2, 2.5,$ and 3 and the corresponding best model fits in the entire frequency range (20 kHz - 45 MHz). (c) Cross-plane thermal conductivity versus film thickness measured in bilayer MoSe₂ (green rhomb), Bi₂Se₃/MoSe₂ SLs (black circles), graphene/PdSe₂ heterostructures (red squares) and Bi₂Se₃ films on STO (purple circles) and sapphire (pink squares) substrates. The blue open triangles show

previously reported k_z values measured in thicker Bi_2Se_3 films.²⁰ By extrapolating the measured k_z trends, we find the minimum film thickness from which phonon-interface scattering starts to have a strong impact on cross-plane heat dissipation, i.e., $k_z(\text{SLs}) < k_z(\text{Bi}_2\text{Se}_3) < k_z(\text{MoSe}_2)$. (d) Total thermal resistance, $R_{\text{tot}} = R_{\text{int}} + R_{\text{film}}$, of $\text{Bi}_2\text{Se}_3/\text{MoSe}_2$ SLs (black solid circles) and graphene/ PdSe_2 heterostructures (red solid squares) versus film thickness. The uncertainty of the estimated R_{tot} was calculated on the basis of error propagation for the input parameters. Total thermal resistance measurements in Au/graphene/ SiO_2 ⁴⁸ (purple open triangles) and Al/graphene- MoS_2 (SLs)/ SiO_2 ⁸ (green open triangles) are included for comparison. The colored lines in (c) and (d) are guides for the eye.

To gain further insight into the influence of phonon-interface scattering on cross-plane thermal conductance, we constructed a tight-binding model⁴⁹ (see details in Methods) and calculated the transmission coefficients of phonons with different frequencies traversing through MoSe_2 , Bi_2Se_3 and $\text{Bi}_2\text{Se}_3/\text{MoSe}_2$ heterostructures from one metallic electrode to the other (see Fig. 4a). The DFT calculations indicate that the Debye frequencies of MoSe_2 and Bi_2Se_3 are 24meV and 48meV, respectively.^{50,51} We adjusted the parameters of our tight-binding model to obtain similar Debye frequencies for both materials (see Fig. S13 in SI). Furthermore, we took into account the lattice mismatch between the heterostructure layers by choosing a different coupling strength and coupling configurations between MoSe_2 and Bi_2Se_3 layers (see details in Figure S13 and Methods). Finally, to consider the effect of thermal contact resistance to electrodes on the overall thermal conductance, we considered two scenarios with weak and strong couplings to electrodes.

Figures 4b,c,d show the calculated k_z of different thickness Bi_2Se_3 , MoSe_2 and $\text{Bi}_2\text{Se}_3/\text{MoSe}_2$ heterostructures as a function of temperature. The k_z increases with increasing temperature and starts to saturate at higher temperatures. Figure 4e shows the room temperature k_z as a function of

film thickness, which is in a good qualitative agreement with the experimental data when we consider a strong coupling between films and electrodes (see blue-shaded area). Specifically, the k_z trends follow a similar order to that in the experiment, and unlike Bi_2Se_3 , the k_z in the SLs varies slowly with thickness. Interestingly, when we consider a weak coupling to electrodes, the calculated absolute k_z values are in much better quantitative agreement with the experiments (see red-shaded area). This suggests that the total interface thermal resistance, R_{int} , is increased when the films are weakly coupled with the top and bottom electrodes, confirming the relative high R_{int} values obtained from FDTR experiments (see Fig. S9). These results highlight the role of thermal contact resistance in cross-plane thermal conductivity of ultra-thin vdW layered materials.

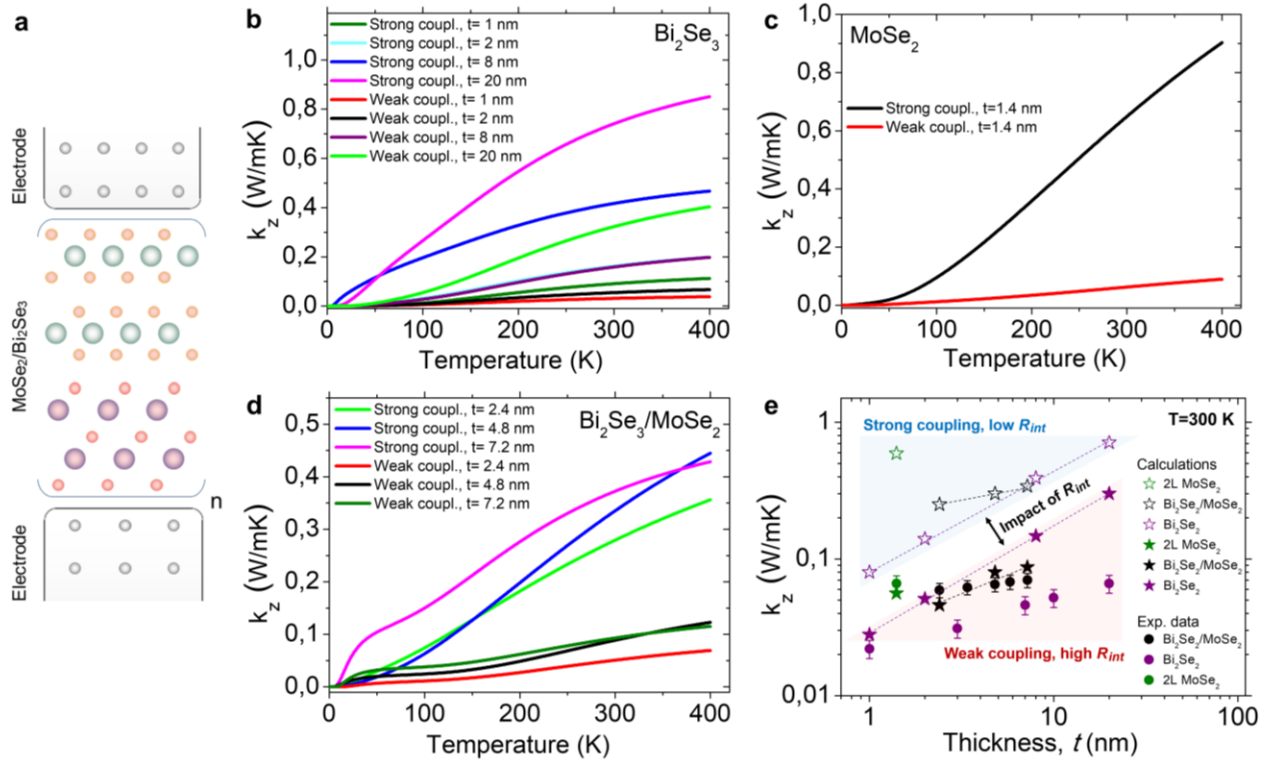


Fig. 4. Tight-binding phonon calculations. (a) Schematic structure of a $\text{Bi}_2\text{Se}_3/\text{MoSe}_2$ vdW layered structure between electrodes. The calculated cross-plane thermal conductivity of (b) Bi_2Se_3 , (c) bilayer MoSe_2 and (d) $\text{Bi}_2\text{Se}_3/\text{MoSe}_2$ heterostructures of different thickness as a

function of temperature (0-400 K) considering weak and strong coupling of the vdW films with the electrodes. (e) The calculated room temperature cross-plane thermal conductivity as a function of thickness for MoSe₂, Bi₂Se₃ and Bi₂Se₃/MoSe₂ heterostructures with weak (solid star symbols) and strong (open star symbols) coupling with the electrodes. The experimental k_z values for MoSe₂, Bi₂Se₃ and Bi₂Se₃/MoSe₂ are shown with green, purple and black solid circles in (e) for direct comparison with the calculations. The difference in the calculated values indicated in blue and red shaded areas in (e) show the importance of quantifying interfacial thermal transport in vdW films bonded to a substrate.

In summary, we have successfully developed ultra-thin epitaxial vdW films that can act as highly insulating thermal metamaterials, comprising of dissimilar atomically thin layers of 2D semiconductors (MoSe₂ and PdSe₂), the 3D topological insulator Bi₂Se₃, and monolayer graphene. Our study reveals that short period crystalline Bi₂Se₃/MoSe₂ superlattices can be used to achieve a superior thermal resistance up to 202 m²K/GW and ultralow effective cross-plane thermal conductivity at room temperature down to 0.059 W/mK. We attribute this result to the interface roughness and large lattice mismatch between the constituent layers of the superlattices that boosts phonon-interface scattering and suppress cross-plane heat dissipation. Conversely, graphene/PdSe₂ heterostructures exhibit a strong thickness-dependent effective cross-plane thermal conductivity and a constant total thermal resistance of about 70 m²K/GW due to ballistic thermal transport. Given the sub-3 nm thickness of these heterostructures, their effective thermal conductivities at room temperature are estimated between 0.012 and 0.06 W/mK. Our phonon transport calculations align well with the experimental results and further shed light on the impact of interfacial thermal resistances between ultra-thin heterointerfaces and top and bottom metallic contacts on cross-plane heat dissipation.

Importantly, this work has yielded significant advancements in the epitaxial growth of high-quality heterogeneous interfaces over large areas, as well as in the quantitative understanding of interfacial thermal transport across atomically-thin vdW films on various substrates. The implications of these findings are extensive for the design of heat-sensitive electronic components and 2D electronic devices, such as 2D transistors and microchips, that can operate without thermal limitations e.g., overheating. The ability to obstruct heat dissipation in the vertical direction while maintaining in-plane crystallinity in wafer-scale engineered vdW stacks not only facilitates thermal management applications but also enhances their suitability as active materials in thermoelectric devices, thereby increasing their thermoelectric efficiency. Combining with bandgap engineering strategies, the followed phonon engineering approach could provide a promising route to realize a wide variety of functional semiconductor heterojunctions and superlattices for nanoscale electronic and thermoelectric devices.

Methods

MBE growth and in-situ characterization (XPS, STM)

The experiments were carried out in an ultrahigh vacuum MBE system equipped with RHEED, X-ray photoelectron spectrometer and scanning tunneling microscope. High purity metals Mo and Pd were evaporated from an e-gun evaporator whereas Se and Bi were evaporated from effusion cells. The Bi_2Se_3 and MoSe_2 films were grown on STO (111) and sapphire substrates at $\sim 300^\circ\text{C}$ under Se-rich conditions with a Se/Mo (Bi, Pd) flux ratio of about 20. The PdSe_2 films were grown on 4H-SiC (0001)/monolayer graphene substrates at $\sim 240^\circ\text{C}$ under Se-rich conditions. The Mo, Bi and Pd growth rates were kept constant at $\sim 0.1\text{\AA}/\text{sec}$. In-situ XPS measurements were performed with excitation by Mg $K\alpha$ radiation (1253.6 eV) using a SPECS XR50 source. After PdSe_2 growth, the samples were transferred to the STM chamber without breaking the vacuum for

in-situ STM characterization. STM images were obtained at room temperature using a Pt/Ir tip. The scanning conditions were $V=0.4$ Volt and $I=400$ pA.

Raman spectroscopy

The Raman spectra were recorded using a customized setup using a Monovista Raman spectrometer manufactured by Princeton and ensembled by S&I GmbH. It was used in a single grating mode (2400 lines) with a spectral resolution better than 0.4 cm^{-1} . The laser line was rejected using a Bragg filter around $\pm 5\text{ cm}^{-1}$. The samples were placed in an automatic xyz stage. Then, a green diode laser ($\lambda = 532\text{ nm}$) was focused on the sample using a $100\times$ microscope objective. The power of the laser was kept as low as possible ($<100\text{ }\mu\text{W}$) to avoid any possible effect of self-heating.

Frequency domain thermorefectance

FDTR is an ultra-fast laser based pump-probe technique which can measure thermal properties of bulk, thin films and nanostructured materials. The experimental setup is based on two lasers operating at 488 nm (pump) and 532 nm (probe). The pump beam is modulated in a wide frequency range (20 kHz – 45 MHz), generating a periodic heat flux with a Gaussian spatial distribution on the 2D sample surface. The reflectivity of the sample, which is probed at the same position by the probed laser, changes as a function of the temperature and displays a phase lag compared to the pump signal. The phase response of the reflected probe beam to the thermal wave was recorded using a lock-in amplifier while the pump signal was used as a reference. We also used a $50\times$ objective to repeat the FDTR measurements and obtained consistent results. The measurements were performed under ambient conditions at room temperature ($\sim 22\text{ }^\circ\text{C}$). Before FDTR measurements, 100 nm Au films were deposited on top of the MBE-grown samples and used as transducers.

Computational Method

To model thermal conductance due to phonons, we first construct a tight-binding dynamical matrix of the MoSe₂ and Bi₂Se₃ lattices using the parameters shown in table S1 of the SI. The choice of these parameters is informed by comparing our TB Debye frequency with the Debye frequency computed using density functional theory.^{50,51} We then construct the dynamical matrix of junctions including the layered materials between electrodes. Following the method described in a previous report,⁴⁹ the phonon transmission $T_p(\omega)$ then can be calculated from the relation $T_p(\omega) = \text{Trace}(\Gamma_L^p(\omega)G_p^R(\omega)\Gamma_R^p(\omega)G_p^{R\dagger}(\omega))$ where $\Gamma_{L,R}^p(\omega) = i(\Sigma_{L,R}^p(\omega) - \Sigma_{L,R}^{p\dagger}(\omega))$ describes the level broadening due to the coupling to the left L and right R electrodes, $\Sigma_{L,R}^p(\omega)$ are the retarded self-frequencies associated with this coupling and $G_p^R = (\omega^2 I - D - \Sigma_L^p - \Sigma_R^p)^{-1}$ is the retarded Green's function, where D and I are dynamical and the unit matrices, respectively. The phonon thermal conductance κ_p at temperature T is then calculated from $\kappa_p(T) = (2\pi)^{-1} \int_0^\infty \hbar\omega T_p(\omega)(\partial f_{BE}(\omega, T)/\partial T)d\omega$ where $f_{BE}(\omega, T) = (e^{\hbar\omega/k_B T} - 1)^{-1}$ is the Bose Einstein distribution function, \hbar is reduced Planck's constant and k_B is Boltzmann's constant.

Data availability

The data that support the findings of this study are available from the corresponding author upon request.

References

- 1 Jin, G. et al. Heteroepitaxial van der Waals semiconductor superlattices. *Nat. Nanotechnol.* **16**, 1092-1098 (2021).

- 2 Zhao, B. et al. High-order superlattices by rolling up van der Waals heterostructures. *Nature* **591**, 385-390 (2021).
- 3 Jiang, J. et al. Flexible ferroelectric element based on van der Waals heteroepitaxy. *Sci. Adv.* **3**, e1700121 (2017).
- 4 Ryu, Y. K., Frisenda, R. & Castellanos-Gomez, A. Superlattices based on van der Waals 2D materials. *Chem. Comm.* **55**, 11498-11510 (2019).
- 5 Merrill, D. R., Moore, D. B., Bauers, S. R., Falmbigl, M. & Johnson, D. C. Misfit Layer Compounds and Ferecrystals: Model Systems for Thermoelectric Nanocomposites. *Mater.* **8**, 2000-2029 (2015).
- 6 Jood, P. et al. Microstructural Control and Thermoelectric Properties of Misfit Layered Sulfides (LaS)_{1+m}TS₂ (T = Cr, Nb): The Natural Superlattice Systems. *Chem. Mater.* **26**, 2684-2692 (2014).
- 7 Guo, R., Jho, Y.-D. & Minnich, A. J. Coherent control of thermal phonon transport in van der Waals superlattices. *Nanoscale* **10**, 14432-14440 (2018).
- 8 Sood, A. et al. Engineering Thermal Transport across Layered Graphene–MoS₂ Superlattices. *ACS Nano* **15**, 19503-19512 (2021).
- 9 Chen, G. & Neagu, M. Thermal conductivity and heat transfer in superlattices. *Appl. Phys. Lett.* **71**, 2761-2763 (1997).
- 10 Lin, Z. et al. High-yield exfoliation of 2D semiconductor monolayers and reassembly of organic/inorganic artificial superlattices. *Chem* **7**, 1887-1902 (2021).
- 11 Wang, C. et al. Monolayer atomic crystal molecular superlattices. *Nature* **555**, 231-236 (2018).

- 12 Vaziri, S. et al. Ultrahigh thermal isolation across heterogeneously layered two-dimensional materials. *Sci. Adv.* **5**, eaax1325 (2019).
- 13 Kim, S. E. et al. Extremely anisotropic van der Waals thermal conductors. *Nature* **597**, 660-665, doi:10.1038/s41586-021-03867-8 (2021).
- 14 Lin, M. et al. Controlled Growth of Atomically Thin In₂Se₃ Flakes by van der Waals Epitaxy. *J. Am. Chem. Soc.* **135**, 13274-13277 (2013).
- 15 Koma, A. Van der Waals epitaxy—a new epitaxial growth method for a highly lattice-mismatched system. *Thin Solid Films* **216**, 72-76 (1992).
- 16 Ravichandran, J. et al. Crossover from incoherent to coherent phonon scattering in epitaxial oxide superlattices. *Nat. Mater.* **13**, 168-172 (2014).
- 17 Nunn, W., Truttmann, T. K. & Jalan, B. A review of molecular-beam epitaxy of wide bandgap complex oxide semiconductors. *J. Mater. Res.* **36**, 4846-4864 (2021).
- 18 Saleta Reig, D. et al. Unraveling Heat Transport and Dissipation in Suspended MoSe₂ from Bulk to Monolayer. *Adv. Mater.* **34**, 2108352 (2022).
- 19 Fournier, D., Marangolo, M., Eddrief, M., Kolesnikov, N. N. & Fretigny, C. Straightforward measurement of anisotropic thermal properties of a Bi₂Se₃ single crystal. *J. Phys. Condens. Matter.* **30**, 115701 (2018).
- 20 Paulatto, L. et al. Thermal conductivity of Bi₂Se₃ from bulk to thin films: Theory and experiment. *Phys. Rev. B* **101**, 205419 (2020).
- 21 Chen, L. et al. In-Plane Anisotropic Thermal Conductivity of Low-Symmetry PdSe₂. *Sustainability* **13**, 4155 (2021).
- 22 Jena, T., Hossain, M. T. & Giri, P. K. Temperature-dependent Raman study and determination of anisotropy ratio and in-plane thermal conductivity of low-temperature

- CVD-grown PdSe₂ using unpolarized laser excitation. *J. Mater. Chem. C* **9**, 16693-16708 (2021).
- 23 Tsipas, P. et al. Observation of Surface Dirac Cone in High-Quality Ultrathin Epitaxial Bi₂Se₃ Topological Insulator on AlN(0001) Dielectric. *ACS Nano* **8**, 6614-6619 (2014).
- 24 Tsipas, P. et al. Epitaxial ZrSe₂/MoSe₂ semiconductor v.d. Waals heterostructures on wide band gap AlN substrates. *Microelectron. Eng.* **147**, 269-272 (2015).
- 25 Le, P. H., Wu, K. H., Luo, C. W. & Leu, J. Growth and characterization of topological insulator Bi₂Se₃ thin films on SrTiO₃ using pulsed laser deposition. *Thin Solid Films* **534**, 659-665 (2013).
- 26 Zhang, J. et al. Raman Spectroscopy of Few-Quintuple Layer Topological Insulator Bi₂Se₃ Nanoplatelets. *Nano Lett.* **11**, 2407-2414 (2011).
- 27 Tonndorf, P. et al. Photoluminescence emission and Raman response of monolayer MoS₂, MoSe₂, and WSe₂. *Opt. Express* **21**, 4908-4916 (2013).
- 28 Varghese, S. et al. Fabrication and characterization of large-area suspended MoSe₂ crystals down to the monolayer. *J. phys. chem. mater.* **4**, 046001 (2021).
- 29 Li, Z. et al. Phonon-assisted electronic states modulation of few-layer PdSe₂ at terahertz frequencies. *npj 2D Mater. Appl.* **5**, 87 (2021).
- 30 Wei, M. et al. Layer-dependent optical and dielectric properties of centimeter-scale PdSe₂ films grown by chemical vapor deposition. *npj 2D Mater. Appl.* **6**, 1 (2022).
- 31 Yu, J. et al. Direct Observation of the Linear Dichroism Transition in Two-Dimensional Palladium Diselenide. *Nano Lett.* **20**, 1172-1182 (2020).
- 32 Yang, H. et al. Self-powered and high-performance all-fiber integrated photodetector based on graphene/palladium diselenide heterostructures. *Opt. Express* **29**, 15631-15640 (2021).

- 33 Bauer, M., Gigler, A. M., Huber, A. J., Hillenbrand, R. & Stark, R. W. Temperature-depending Raman line-shift of silicon carbide. *J. Raman. Spectrosc.* **40**, 1867-1874 (2009).
- 34 El Sachat, A. et al. Effect of crystallinity and thickness on thermal transport in layered PtSe₂. *npj 2D Mater. Appl.* **6**, 32 (2022).
- 35 Xiao, P. et al. Anisotropic Thermal Conductivity of Crystalline Layered SnSe₂. *Nano Lett.* **21**, 9172-9179 (2021).
- 36 Schmidt, A. J., Cheaito, R. & Chiesa, M. A frequency-domain thermoreflectance method for the characterization of thermal properties. *Rev. Sci. Instrum.* **80**, 094901 (2009).
- 37 Bismuth selenide (Bi₂Se₃) Debye temperature, heat capacity: Datasheet from Landolt-Börnstein - Group III Condensed Matter · Volume 41C: "Non-Tetrahedrally Bonded Elements and Binary Compounds I" in SpringerMaterials (https://doi.org/10.1007/10681727_948) (Springer-Verlag Berlin Heidelberg).
- 38 Kiwia, H. L. & Westrum, E. F. Low-temperature heat capacities of molybdenum diselenide and ditelluride. *J. Chem. Thermodyn.* **7**, 683-691 (1975).
- 39 Schmidt, A. J., Chen, X. & Chen, G. Pulse accumulation, radial heat conduction, and anisotropic thermal conductivity in pump-probe transient thermoreflectance. *Rev. Sci. Instrum.* **79**, 114902 (2008).
- 40 Koh, Y. K., Cao, Y., Cahill, D. G. & Jena, D. Heat-Transport Mechanisms in Superlattices. *Adv. Funct. Mater.* **19**, 610-615 (2009).
- 41 Cheaito, R. et al. Experimental Investigation of Size Effects on the Thermal Conductivity of Silicon-Germanium Alloy Thin Films. *Phys. Rev. Lett.* **109**, 195901 (2012).
- 42 Chalopin, Y., Esfarjani, K., Henry, A., Volz, S. & Chen, G. Thermal interface conductance in Si/Ge superlattices by equilibrium molecular dynamics. *Phys. Rev. B* **85**, 195302 (2012).

- 43 Chen, Y., Li, D., Lukes, J. R., Ni, Z. & Chen, M. Minimum superlattice thermal conductivity from molecular dynamics. *Phys. Rev. B* **72**, 174302 (2005).
- 44 Sood, A. et al. Quasi-Ballistic Thermal Transport Across MoS₂ Thin Films. *Nano Lett.* **19**, 2434-2442 (2019).
- 45 Li, X. & Yang, R. Effect of lattice mismatch on phonon transmission and interface thermal conductance across dissimilar material interfaces. *Phys. Rev. B* **86**, 054305 (2012).
- 46 Touzelbaev, M. N., Zhou, P., Venkatasubramanian, R. & Goodson, K. E. Thermal characterization of Bi₂Te₃/Sb₂Te₃ superlattices. *J. Appl. Phys.* **90**, 763-767 (2001).
- 47 Landauer, R. Electrical resistance of disordered one-dimensional lattices. *Philos. Mag. (Abingdon)* **21**, 863-867 (1970).
- 48 Koh, Y. K., Bae, M.-H., Cahill, D. G. & Pop, E. Heat Conduction across Monolayer and Few-Layer Graphenes. *Nano Lett.* **10**, 4363-4368 (2010).
- 49 Sadeghi, H. Theory of electron, phonon and spin transport in nanoscale quantum devices. *Nanotechnology* **29**, 373001 (2018).
- 50 Xiao, Y. et al. Structural evolution and phase transition mechanism of MoSe₂ under high pressure. *Sci. Rep.* **11**, 22090 (2021).
- 51 Wang, B.-T. & Zhang, P. Phonon spectrum and bonding properties of Bi₂Se₃: Role of strong spin-orbit interaction. *Appl. Phys. Lett.* **100**, 082109 (2012).

Acknowledgements

A.E. acknowledges funding from the EU-H2020 research and innovation program under the Marie Skłodowska Curie Individual Fellowship THERMIC (Grant No. 101029727). H.S. acknowledges the UKRI for Future Leaders Fellowship numbers MR/S015329/2 and MR/X015181/1. E.C.A and C.M.S.T. acknowledge support from the project LEIT funded by the European Research Council,

H2020 Grant Agreement No. 885689. ICN2 is supported by the Severo Ochoa program from the Spanish Research Agency (AEI, grant no. SEV-2017-0706) and by the CERCA Programme/Generalitat de Catalunya.

Author contributions

A.E. conceived and supervised the research work. P.T. and A.D. fabricated the MBE samples, performed the XPS measurements and provided inputs in the structural analysis. A.E., E.C.-A. and P.X. performed the Raman and TEM measurements and analysis. A.E. and E.C.-A. built the FDTR setup and performed the thermal measurements and data analysis. M.T.A, A.D. and H.S. performed the thermal conductance calculations and provided support to the theoretical analysis. All authors reviewed and edited the manuscript and have given approval to the final version of the manuscript. The manuscript was written by A.E. with inputs from E.C.-A., P.T., H.S. and C.M.S.T.

Competing interests

The authors declare no competing interests

Additional Information

Supplementary Information: RHEED patterns; XPS spectra; FDTR sensitivity analysis; FDTR experimental data; Raman experimental data; Tight-binding phonon calculations;

Correspondence and requests for materials should be addressed to Alexandros El Sachat.

Supporting Information:

Engineering heat transport across epitaxial lattice-mismatched van der Waals heterointerfaces

Emigdio Chavez-Angel,¹ Polychronis Tsipas,² Peng Xiao,¹ Mohammad Taghi Ahmadi,³ Abdalghani Daaoub,³ Hatef Sadeghi,³ Clivia M. Sotomayor Torres,^{1,4} Athanasios Dimoulas² and Alexandros El Sachat^{1,2}*

¹ Catalan Institute of Nanoscience and Nanotechnology (ICN2), CSIC and BIST, Campus UAB, Bellaterra, 08193 Barcelona, Spain

² Institute of Nanoscience and Nanotechnology, National Center for Scientific Research “Demokritos”, 15341 Agia Paraskevi, Athens, Greece

³ School of Engineering, University of Warwick, CV4 7AL Coventry, United Kingdom

⁴ ICREA, Passeig Lluís Companys 23, 08010 Barcelona, Spain

*Corresponding author: a.elsachat@inn.demokritos.gr

1. RHEED patterns and XPS data

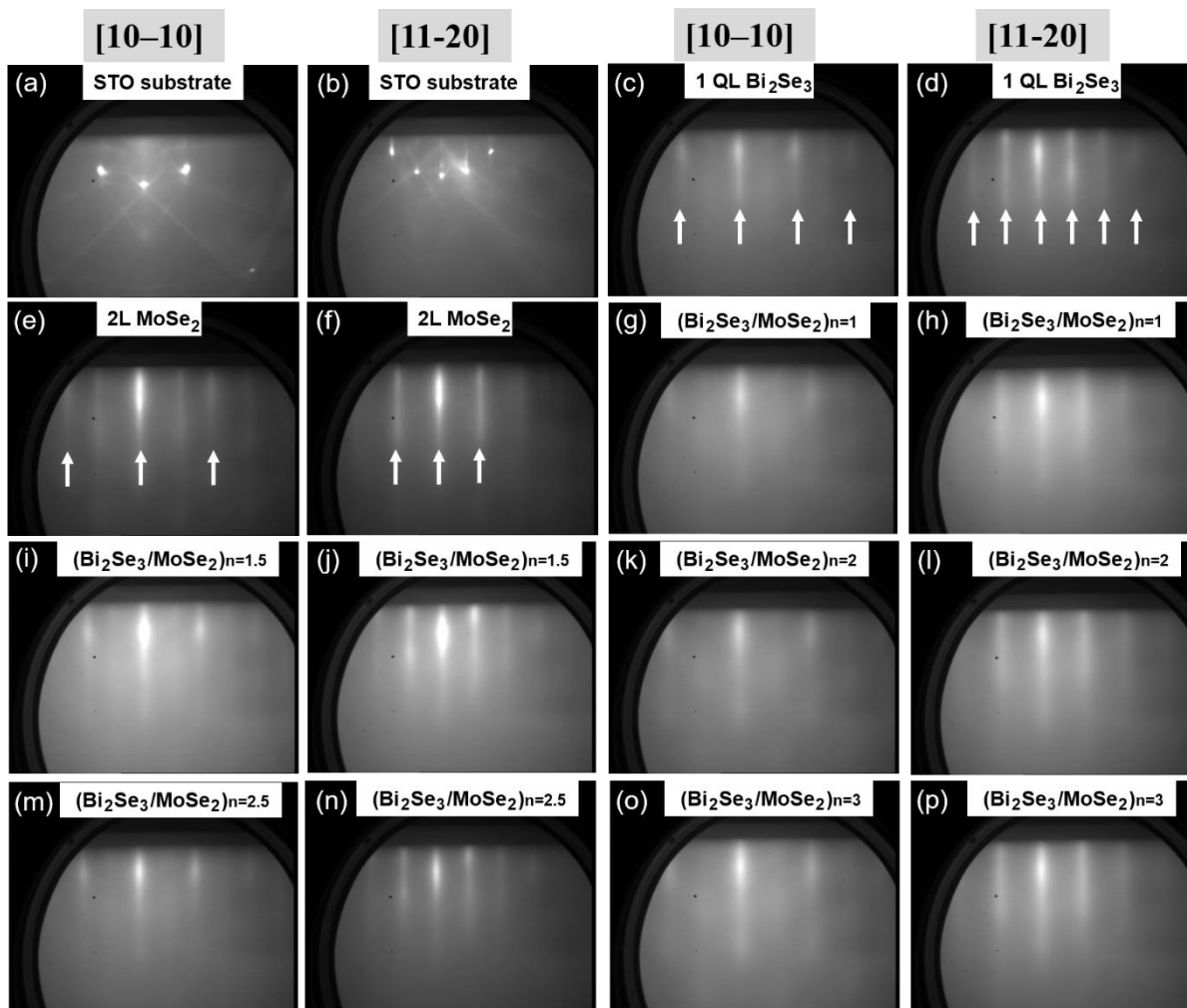


Fig. S1. RHEED patterns of all the Bi₂Se₃/MoSe₂ films along the [10-10] and [11-20] azimuths. The white arrows in (c), (d) and (e), (f) show Bi₂Se₃ and MoSe₂ streaks, respectively.

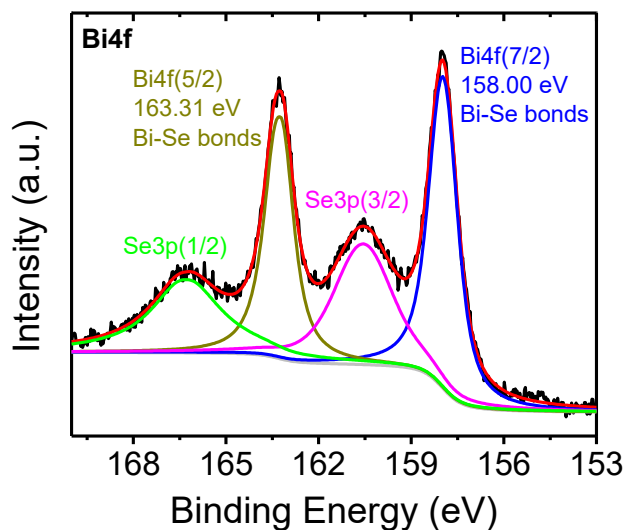


Fig. S2. XPS spectra in Bi₂Se₃/MoSe₂ heterostructure grown on STO substrate, showing that the Bi 4f (7/2) peak position remains unaffected after MoSe₂ film growth.

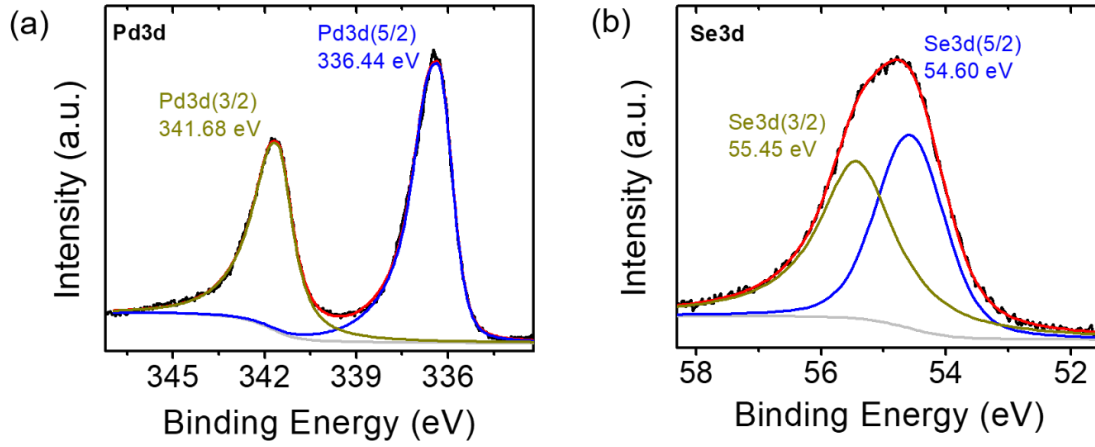


Fig. S3. (a) XPS data showing the Pd 3d (5/2) (336.44 eV) and Pd 3d (3/2) (341.68) core levels and Se 3d electrons. The Se 3d (5/2) (blue) and Se 3d (3/2) (yellow) peaks are overlapped and shown as one peak (black). No reaction with the substrate is observed and the positions and line shapes of the Pd 3d and Se 3d peaks indicate Pd–Se bonding.

2. FDTR sensitivity analysis and experimental data

For the sensitive analysis, we used a polynomial fit of the experimental thickness dependence of the cross-plane thermal conductivity (k_z). This fit allows us to have a continuous function to plot the sensitivity as a function of excitation frequency (20 kHz–45 MHz) and sample thickness. From Fig. S4a,b and Fig. S5ab we find that the sensitivity of the phase signal to $G_{12} = 1/R_1$ and $G_{23} = 1/R_2$ is relatively low and mainly at high frequencies. However, the sensitivity of the phase signal to k_z is high in all the frequency range (Fig. S4d and Fig. S5d). In our measurements, the error bars of the k_z , were estimated by the standard deviation of several measurements, including the numerical errors from the fits (see Fig. S6-S8).

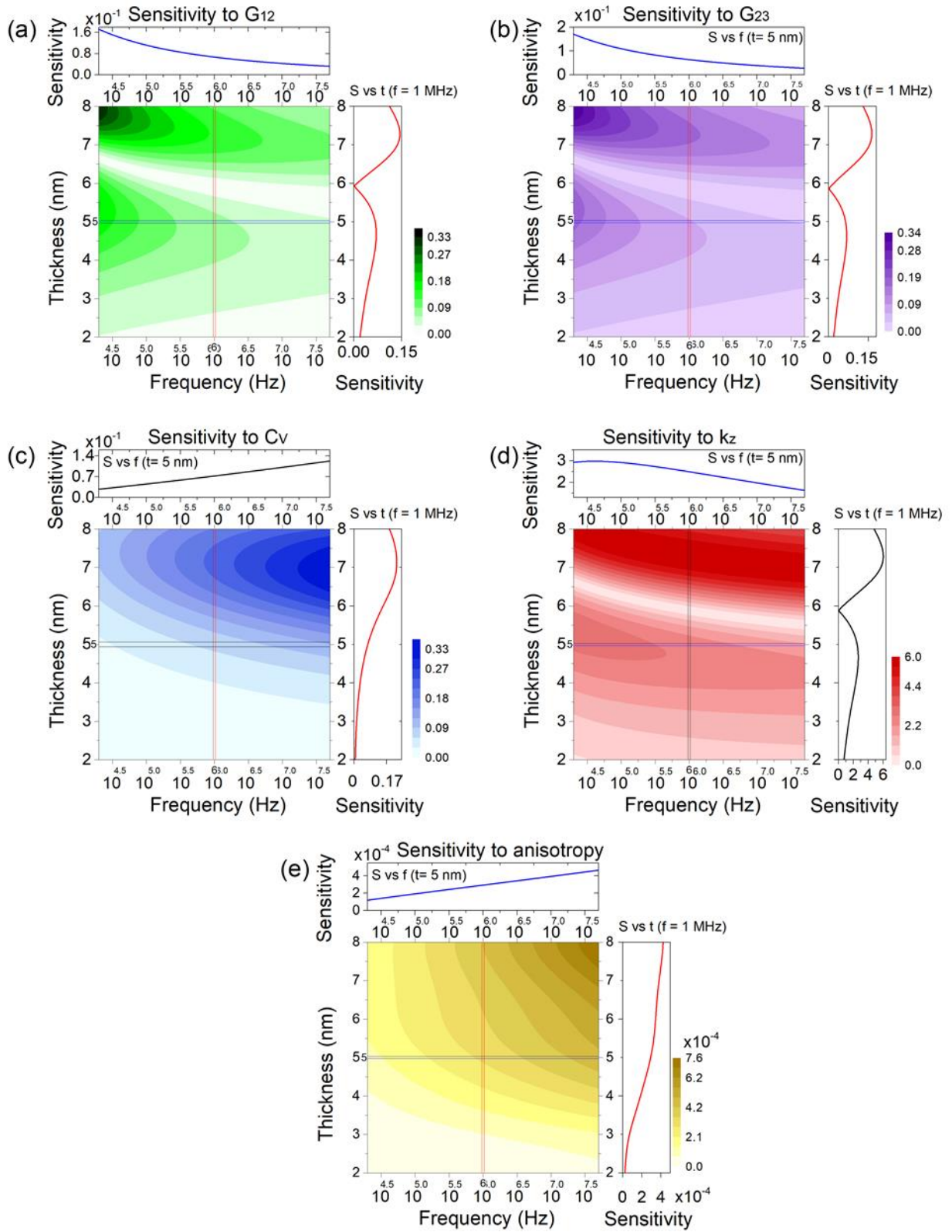


Fig. S4. Calculated phase sensitivity ($-V_{in}/V_{out}$) to different parameters, (a) $G_{12}=1/R_1$ (b) $G_{23}=1/R_2$ (c) C_v , (d) k_z , and (e) anisotropy as a function of thickness and modulation frequency for the case of Au/SLs/STO stacks.

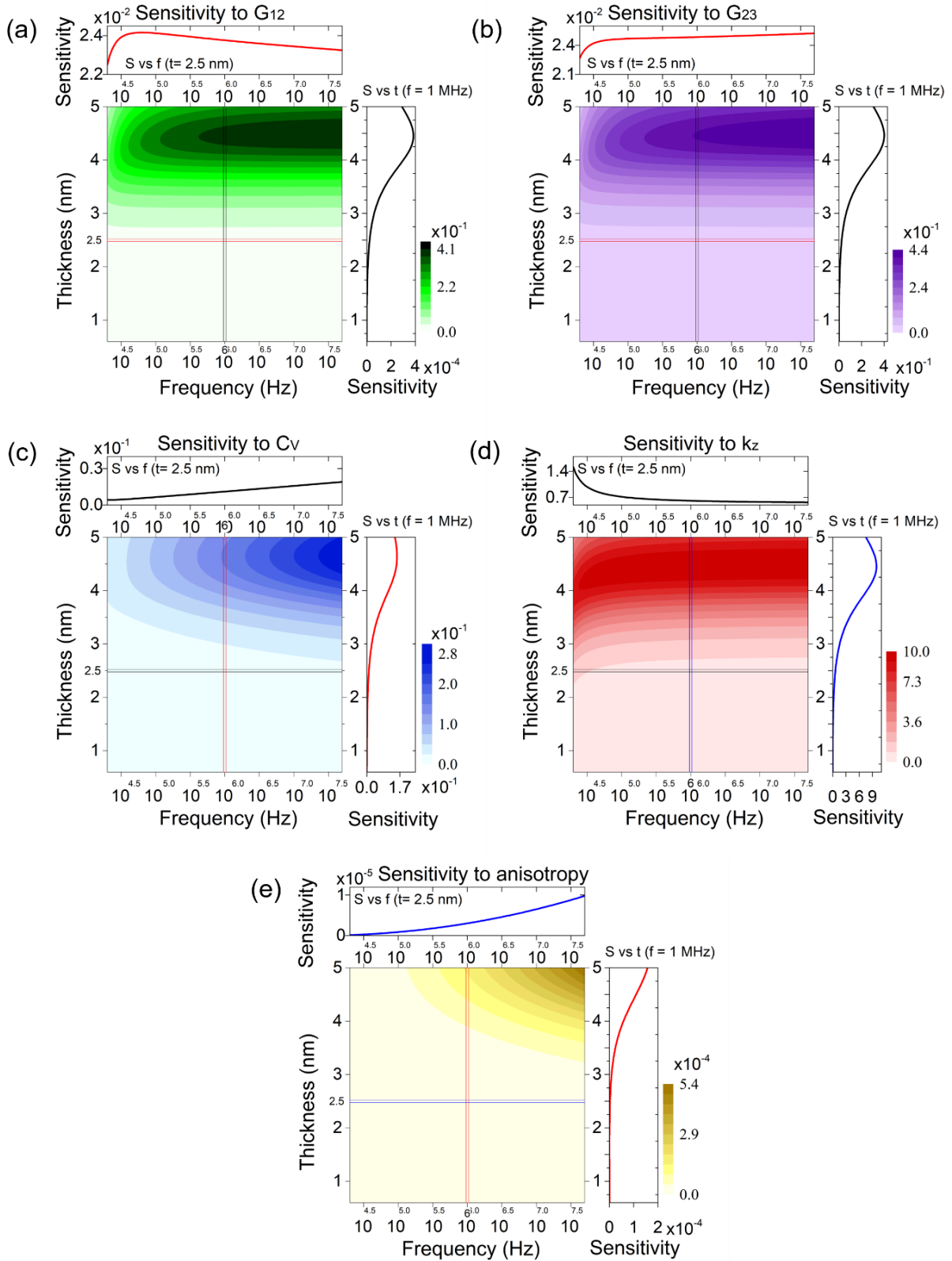


Fig. S5. Calculated phase sensitivity ($-V_{in}/V_{out}$) to different parameters, (a) G_{12} , (b) G_{23} , (c) C_v , (d) k_z , and (e) anisotropy as a function of thickness and modulation frequency for the case of Au/PdSe₂/graphene/SiC stacks.

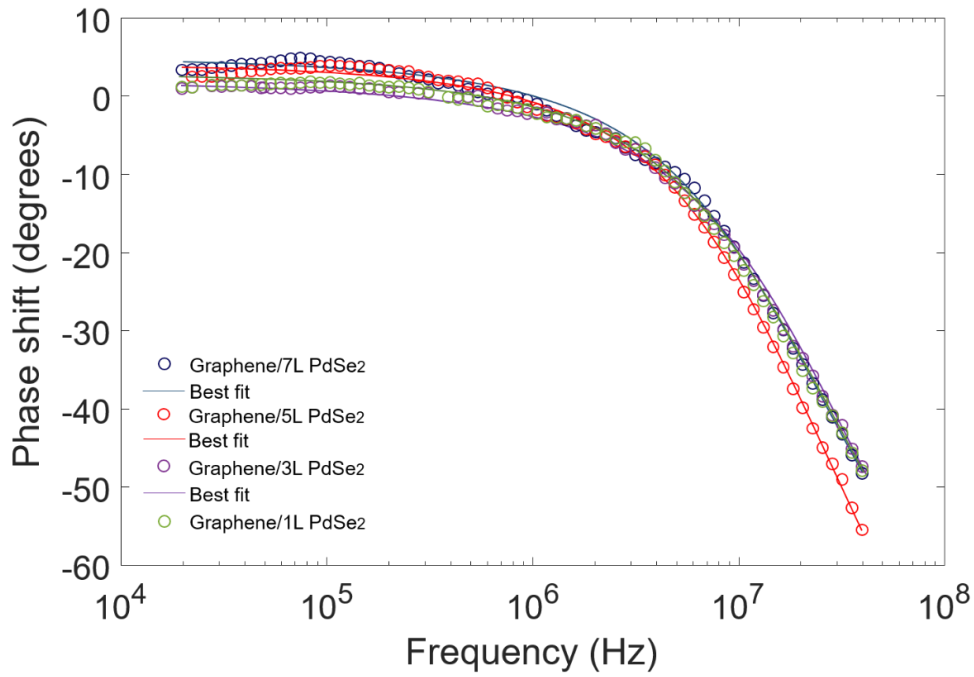


Fig. S6. FDTR data sets measured in graphene/PdSe₂ films of different thickness grown on silicon carbide and the corresponding best model fits in the whole frequency range (20 kHz-45 MHz).

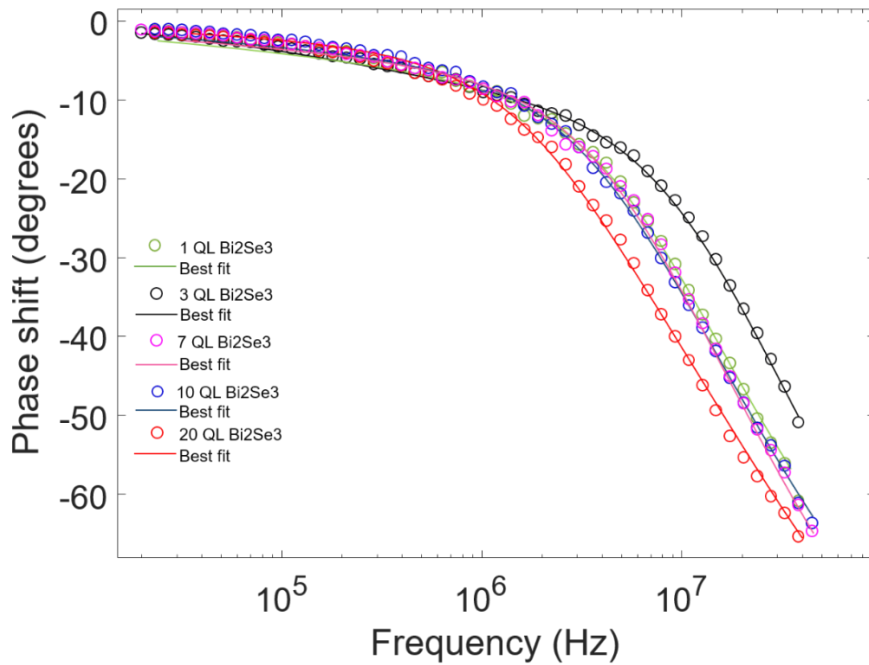


Fig. S7. FDTR data sets measured in 1, 3, 7, 10 and 20 QL Bi₂Se₃ films on sapphire substrate and the corresponding best model fits in the whole frequency range (20 kHz-45 MHz).

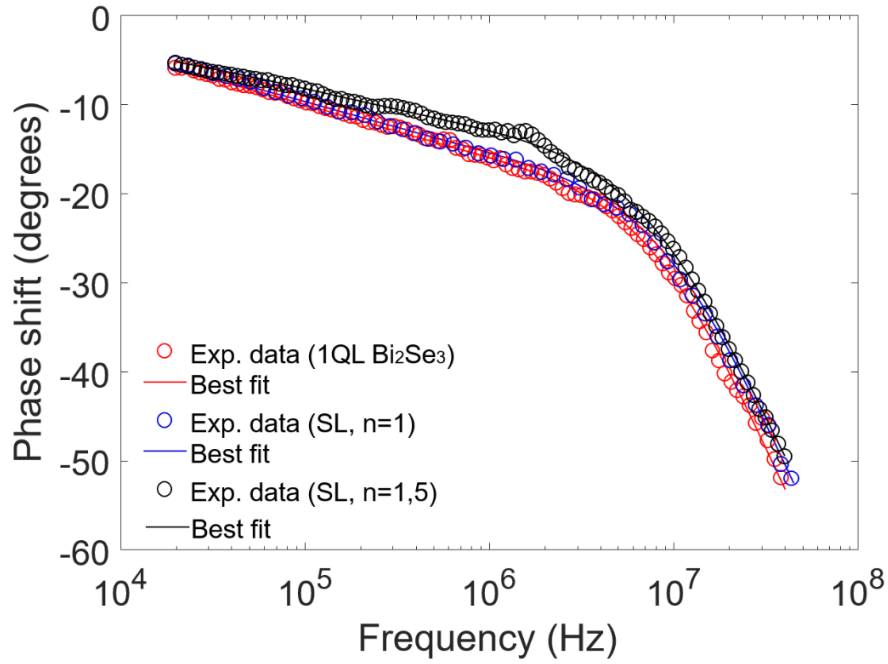


Fig. S8. FDTR data measured in 1 QL Bi_2Se_3 (red circles) and layered $\text{Bi}_2\text{Se}_3/\text{MoSe}_2$ SLs with periods $n = 1, 1.5$ and the corresponding best model fits in the whole frequency range (20 kHz-45 MHz).

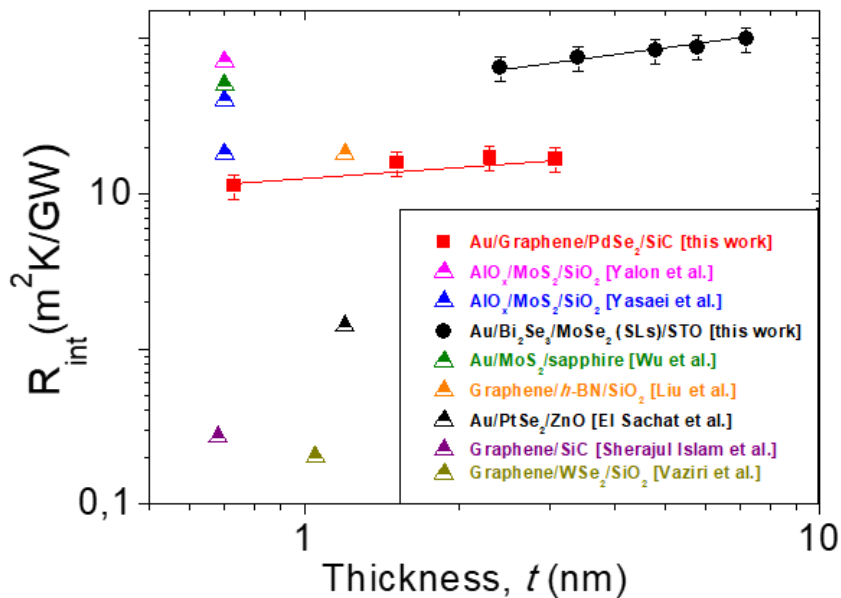


Fig. S9. Total interface thermal resistance values, $R_{\text{int}}=R_1+R_2$, extracted by the FDTR measurements taking into account the multilayer geometry of $\text{Bi}_2\text{Se}_3/\text{MoSe}_2$ SLs and graphene/ PdSe_2 heterostructures. The errors bars estimated by the standard deviation of several

measurements, including the numerical errors from the fits. For comparison, we plot previous interface thermal resistance values measured in 2D/2D and 3D/2D interfaces.¹⁻⁷

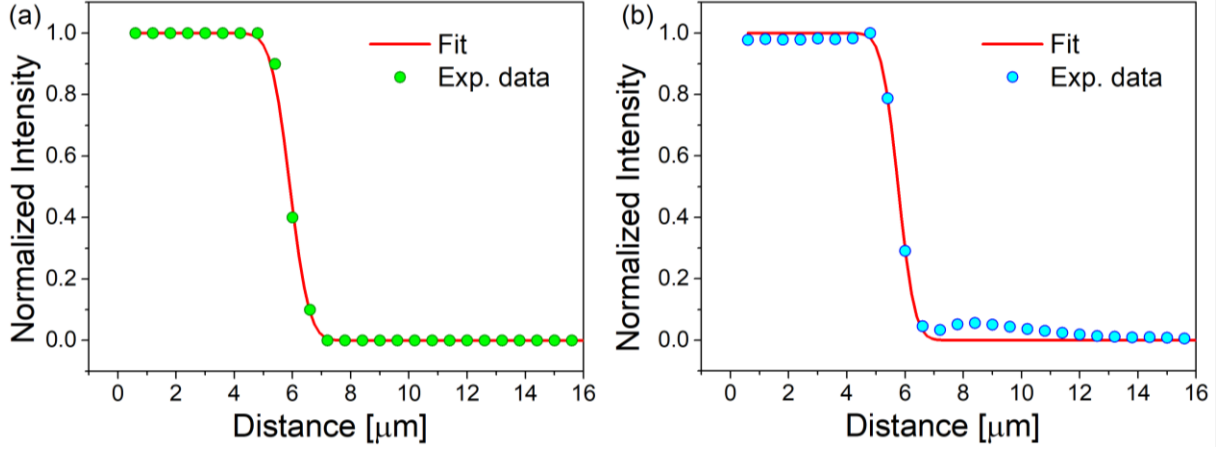


Fig. S10. Typical examples of measured (a) pump and (b) probe spot sizes in Au/ Bi_2Se_3 /MoSe₂ (SLs)/STO stacks. The spot size of each measurement was measured by using the knife's edge method. The edge of the Au transducer layer was used as a sharp edge to measure the intensity of the reflected light as a function of stage position. The beam intensity as a function of translation distance was fitted to an error function curve⁸ and the $1/e^2$ radius of this curve was taken as the laser spot radius.

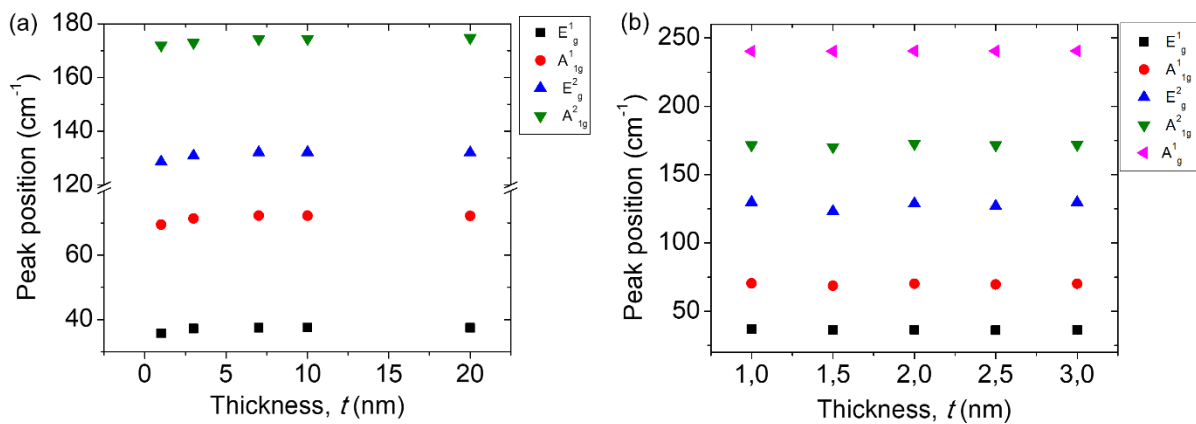


Fig. S11. Peak position of all the Raman active modes versus thickness in (a) Bi_2Se_3 films and (b) $\text{Bi}_2\text{Se}_3/\text{MoSe}_2$ SLs.

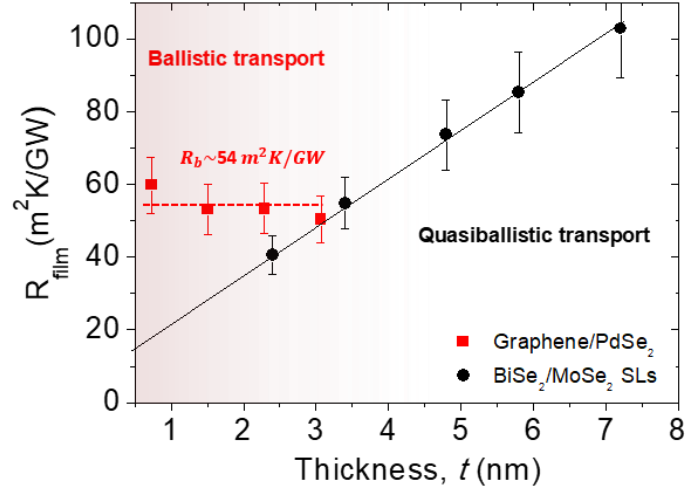


Fig. S12. The volumetric cross-plane thermal resistance, $R_{\text{film}} = t/k_z$, as a function of film thickness t for the Bi₂Se₃/MoSe₂ SLs (black solid circles) and graphene/PdSe₂ heterostructures (red solid squares).

3. Tight-binding phonon calculations

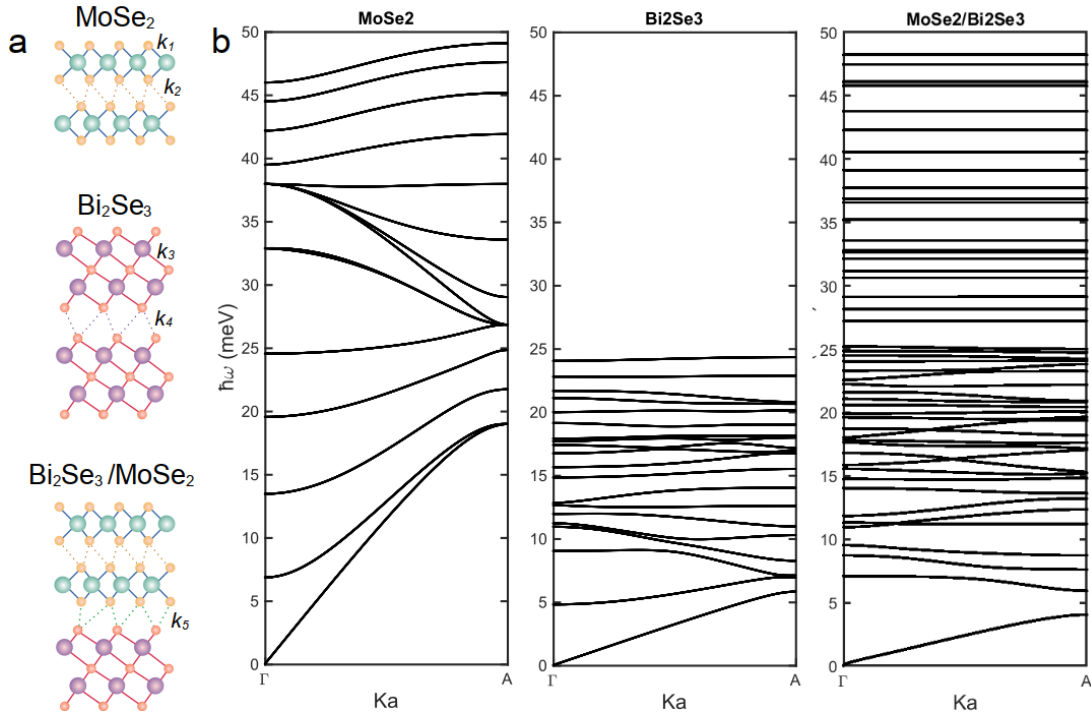


Fig. S13. Tight-binding phonon band structure. (a) The schematic structure of layers vdW structures, phonon band structure of (b) MoSe₂, (c) Bi₂Se₃ and (d) Bi₂Se₃/MoSe₂ hetero structure.

Table S1. The parameters used for to construct the tight binding model with respect to the reference energy t .

Force constant	k_1	k_2	k_3	k_4	k_5
		t	t	$t/5$	$t/6$

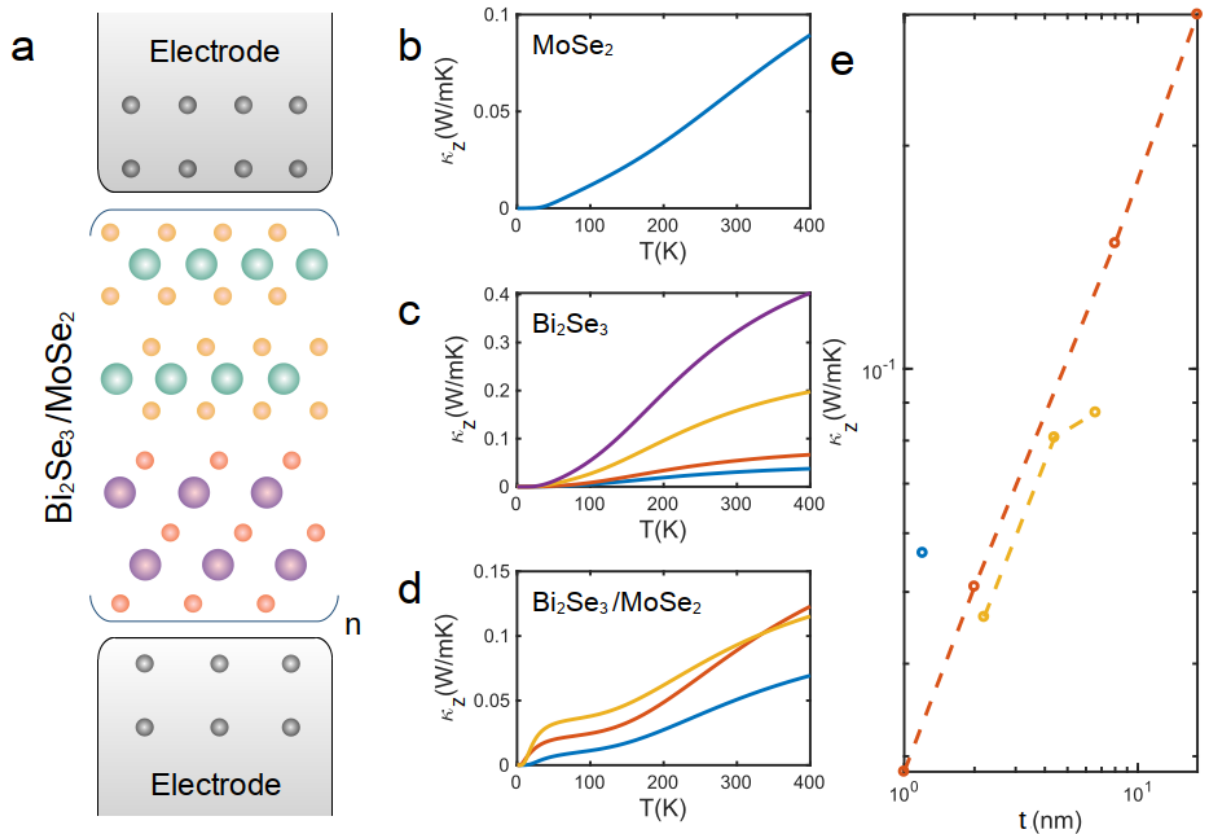


Fig. S14. Calculated cross-plane thermal conductivity of MoSe_2 , Bi_2Se_3 and $\text{Bi}_2\text{Se}_3/\text{MoSe}_2$ heterostructures considering a weak coupling with the electrodes. (a) The schematic structure of layers vdW structures between electrodes. The thermal conductivity as a function of temperature of (b) MoSe_2 , (c) Bi_2Se_3 and (d) $\text{Bi}_2\text{Se}_3/\text{MoSe}_2$ heterostructures. (e) The thermal conductivity as a function of thickness for MoSe_2 , Bi_2Se_3 and $\text{Bi}_2\text{Se}_3/\text{MoSe}_2$ heterostructures at room temperature.

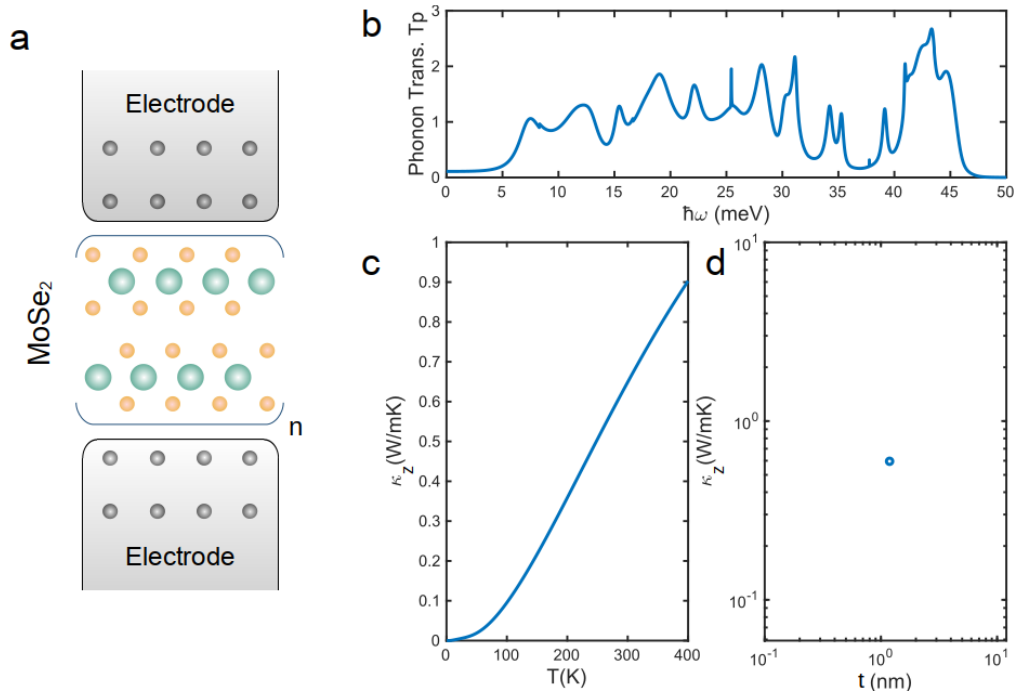


Fig. S15. Calculated cross-plane thermal conductivity of MoSe₂ considering a strong coupling with the electrodes. (a) The schematic structure of MoSe₂ between electrodes, (b) phonon transmission coefficient as a function of phonon energy, (c) thermal conductivity as a function of temperature and (d) thermal conductivity as a function of thickness at room temperature.

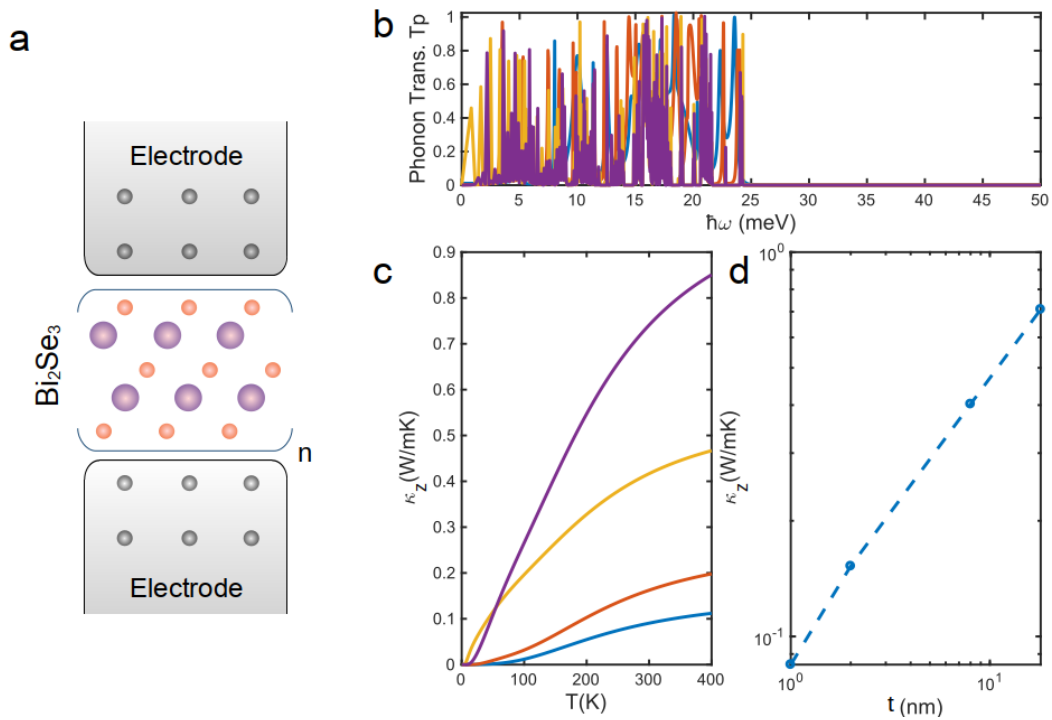


Fig. S16. Calculated cross-plane thermal conductivity of Bi_2Se_3 considering a strong coupling with the electrodes. (a) The schematic structure of Bi_2Se_3 between electrodes, (b) phonon transmission coefficient as a function of phonon energy, (c) thermal conductivity as a function of temperature and (d) thermal conductivity as a function of thickness at room temperature.

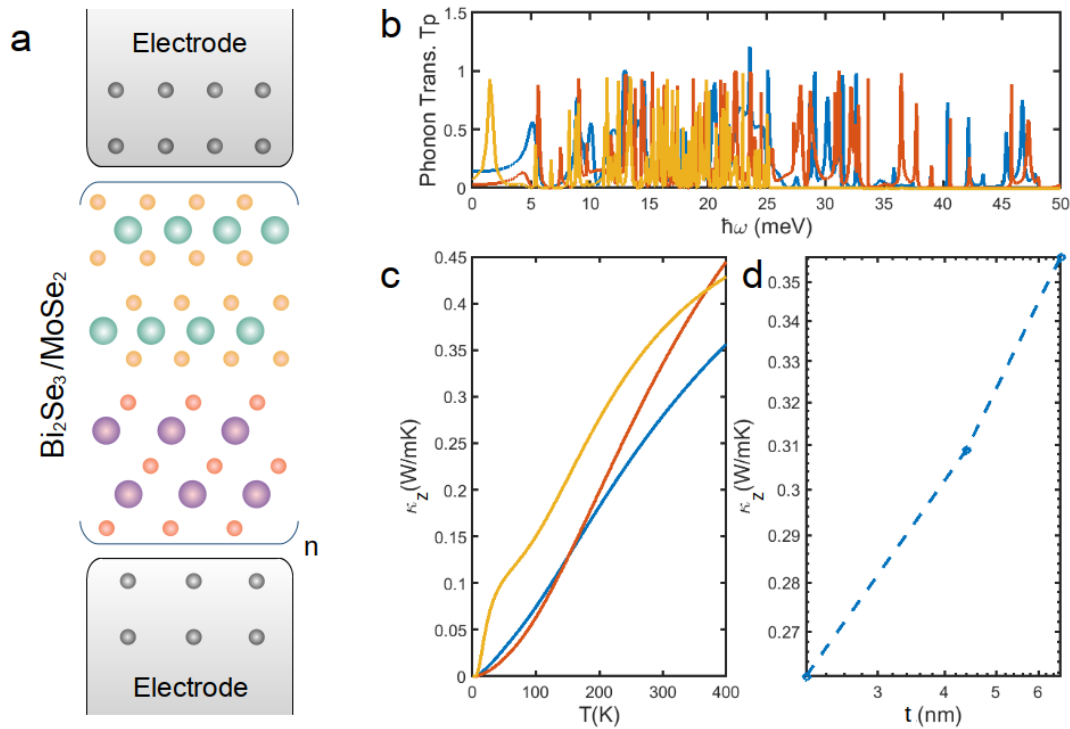


Fig. S17. Calculated cross-plane thermal conductivity of $\text{Bi}_2\text{Se}_3/\text{MoSe}_2$ heterostructures considering a strong coupling with the electrodes. (a) The schematic structure of $\text{Bi}_2\text{Se}_3/\text{MoSe}_2$ between electrodes, (b) phonon transmission coefficient as a function of phonon energy, (c) thermal conductivity as a function of temperature and (d) thermal conductivity as a function of thickness at room temperature.

References

- 1 Yalon, E. et al. Temperature-Dependent Thermal Boundary Conductance of Monolayer MoS_2 by Raman Thermometry. *ACS Appl. Mater. Interfaces* **9**, 43013-43020 (2017).

- 2 Yasaei, P. et al. Interfacial Thermal Transport in Monolayer MoS₂- and Graphene-Based Devices. *Adv. Mater. Interfaces* **4**, 1700334 (2017).
- 3 El Sachat, A. et al. Effect of crystallinity and thickness on thermal transport in layered PtSe₂. *npj 2D Mater. Appl.* **6**, 32 (2022).
- 4 Wu, Y.-J. et al. Tuning Interfacial Thermal and Electrical Conductance across a Metal/MoS₂ Monolayer through N-Methyl-2-pyrrolidone Wet Cleaning. *Adv. Mater. Interfaces* **7**, 2000364 (2020).
- 5 Liu, Y. et al. Thermal Conductance of the 2D MoS₂/h-BN and graphene/h-BN Interfaces. *Sci. Rep.* **7**, 43886 (2017).
- 6 Islam, M. S., Mia, I., Islam, A. S. M. J., Stampfl, C. & Park, J. Temperature and interlayer coupling induced thermal transport across graphene/2D-SiC van der Waals heterostructure. *Sci. Rep.* **12**, 761 (2022).
- 7 Vaziri, S. et al. Ultrahigh thermal isolation across heterogeneously layered two-dimensional materials. *Sci. Adv.* **5**, eaax1325 (2019).
- 8 Nemoto, S. Measurement of the refractive index of liquid using laser beam displacement. *Appl. Opt.* **31**, 6690-6694, doi:10.1364/AO.31.006690 (1992).